Project Number: 766566

Project Acronym: ASPIN

Project title: Antiferromagnetic Spintronics

Periodic Technical Report

Part B

Period covered by the report: from 01/10/2017 to 30/09/2018

Periodic report: 1st

Contents

1 Explanation of the work carried out by the beneficiaries and Overview of the progress

1.1 Objectives

The three research Work packages WP1-WP3 reflect the three intertwined project research areas with their respective Objectives and Milestones.

1.2 Explanation of the work carried per WP

1.2.1 Work Package WP1, Objective O1: Spintronics memory-logic

Contributing teams:

- IOP: CuMnAs/Si, CuMnAs/GaAs thin-film growth and characterization, bit-cell device fabrication, electrical measurements, theory
- NOT: CuMnAs/GaP, Fe/CuMnAs/GaP thin-film growth and characterization, magnetization measurements, XMLD-PEEM measurements
- MPG: Mn_3Sn thin-film growth and characterization, theory
- IGS: PCB design, IoT development site
- JGU: Mn_2Au thin-film growth and characterization, electrical measurements, theory

Fig. 1 shows in a nutshell the scope of WP1 with the most extensively employed thin-film antiferromagnet CuMnAs, typical cross-shape memory bit-cell, and the possibility to electrically write/read the memory state by a PC via a USB-connected printed circuit board (for details see Ref. [1]).

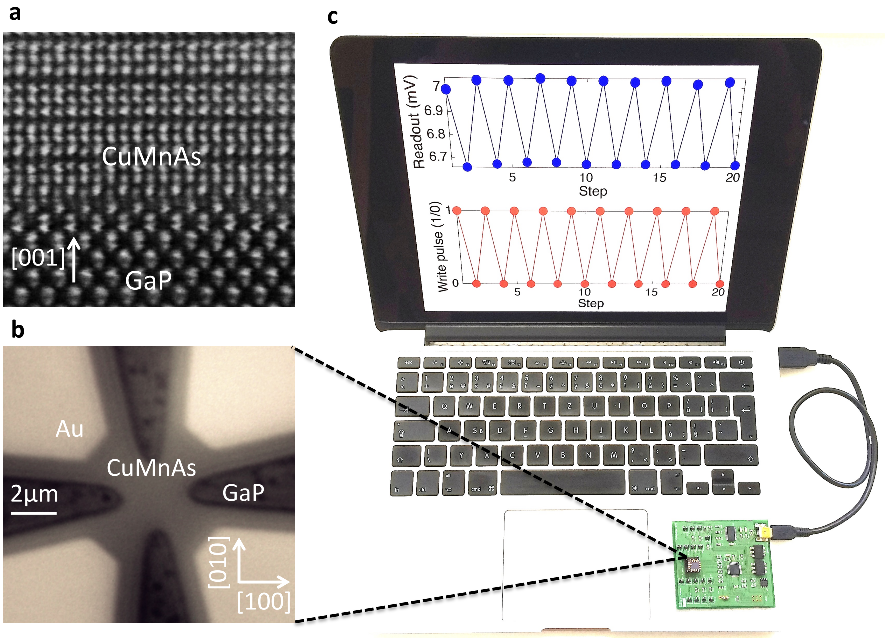

Figure 1: (a) Antiferromagnetic CuMnAs thin film. (b) Memory bit-cell operated from a PC via (c) a USB connected board. From Ref. [1]

Objective O1.2: Spin-torque writing. Following our discovery of the current-induced spin-orbit torque switching in anitferromagnetic CuMnAs from before ASPIN project submission (for the principle see Figs. 2A,B and for more details Refs. [2, 3]), we have performed a systematic study of current and energy densities required for switching with the following key results:

- At writing pulse length τ_p ∼ns, which is at the limit of present ferromagnetic MRAMs, our switching current density is $\sim 10^8$ Acm^{-2} and energy density $\sim$ kJcm^{-3} (see Fig. 3). This is comparable to the common Co/Pt based ferromagnetic spin-orbit torque devices (for more details see Ref. [4]).
- The breakdown margin is sufficiently large (see Fig. 3), allowing us to demonstrate tens of thousands of reversible writing cycles without any notable wear-out of our experimental devices [1, 4].
- The reversible switching by the current-induced spin-orbit torque in our devices is heat assisted (see Fig. 4). We observe increase of the temperature until the first ~ 10 μs followed by a saturated regime connected with establishing thermal gradient in the substrate below the device. We also observe that the current density increases significantly with decreasing base temperature while the temperature at the end of the pulse is similar (see Fig. 4). This is consistent with the observed saturation of the writing energy at shorter pulses (below ∼10 ns) during which heat does not have time to dissipate from the device (see Fig. 3). In this regime the transient increase of sample temperature during the pulse can be expected to scale with the delivered energy (for more details see Ref. [4]).

- We have achieved switching with 1 ps pulses at the same switching energy is in the ns-range. More details are in Ref. [4] and below in WP2.

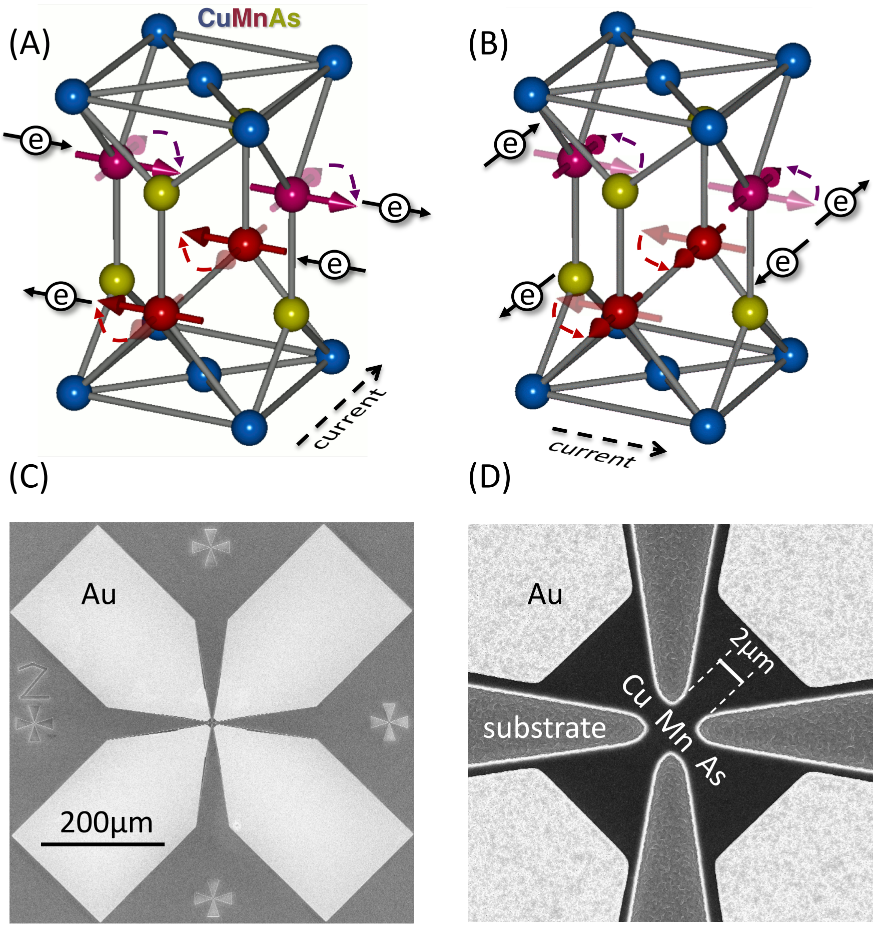

Figure 2: (A,B) Principle of reversible 90° switching by antiferromagnetic current-induced spin-orbit torque. (C,D) Cross-shape bit-cell microdevice. From Ref. [4]

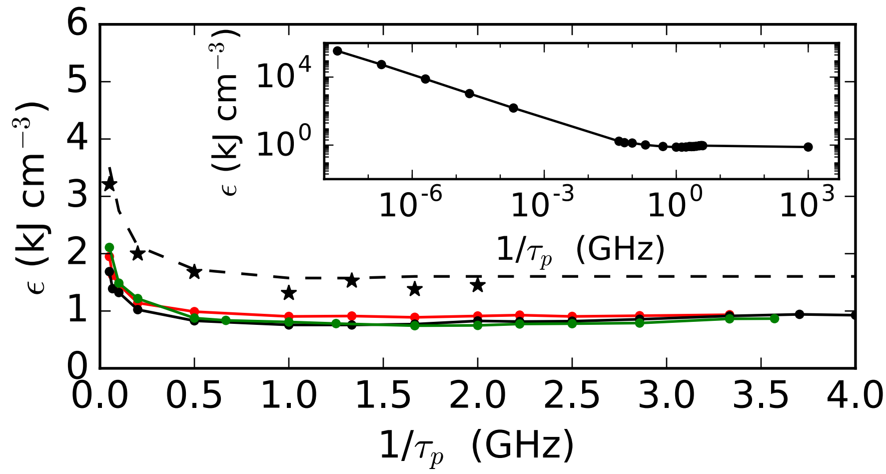

Figure 3: Writing energy density (black, red, and green dots), $\epsilon = j^2\tau_p/\sigma$, required to obtain a 1 mΩ switching signal as a function of the writing speed $1/\tau_p$ in the linear scale (main plot) and in the log-log scale (inset). Black dots in the main plot correspond to 2 μm, red to 3 μm, and green to 4 μm size CuMnAs/GaAs bit cells. Black star-symbols and dashed line represent the limiting breakdown energy density. From Ref. [4]

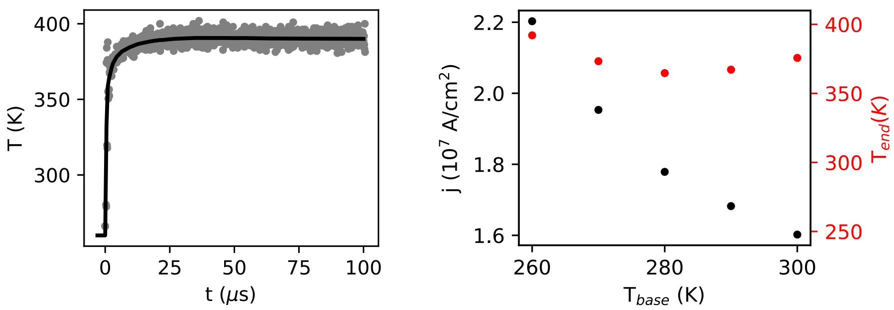

Figure 4: Device temperature with the pulse on. Left panel: An example of the evolution of the temperature of the device determined from resistance measurements during a 100 μs long writing pulse of current density 2.2×10^7 Acm^{-2} and base temperature 260 K. Right panel: Current density (black) needed to write a 5 mΩ signal and temperature of the device at the end of the writing pulse (red) as a function of the base temparture. From Ref. [4]

Objective O1.2: Magnetoresistive readout. Following our demonstration of the anisotropic magnetoresistance (AMR) readout of the 90° switching in anitferromagnetic CuMnAs from before the ASPIN project submission (see Ref. [3]), we have performed a systematic study of the resistive readout signals with the following key results:

- The resistive readout signal can reach Ohm scales in micron-size devices, corresponding to AMR ratios approaching a ∼10% range. This makes it directly usable in standard PCBs powered from a 3 V USB interface.
- We have discovered a new second-order magneto-transport effect, relying on broken time-reversal and space-inversion symmetries in antiferromagnetic CuMnAs crystals, that allowed us to electrically detect 180° Néel vector reversal (see Fig. 6 and for more details Ref. [5]). The detection signal scales with the readout current and is ∼ 0.1 mΩ at 1 mA which makes it directly detectable by common electrical set-ups. This opens the possibility of further exploring the 180° switching mode which is the mode used in ferromagnetic memory devices.

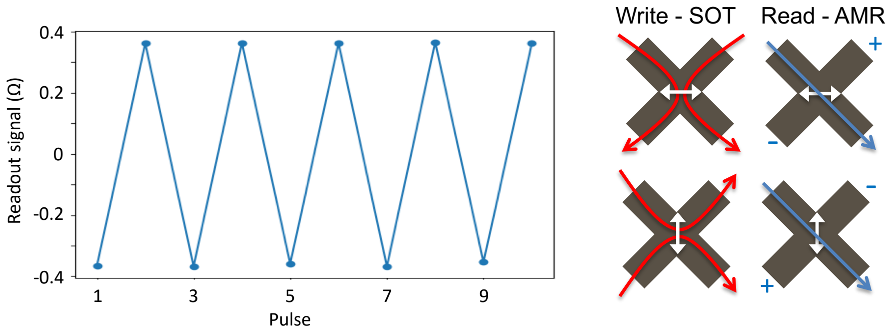

Figure 5: Digital mode of an antiferromagnetic memory cell with 90° switching and AMR readout. One writing pulse in one direction is followed by one pulse in the orthogonal direction. From Ref. [6]

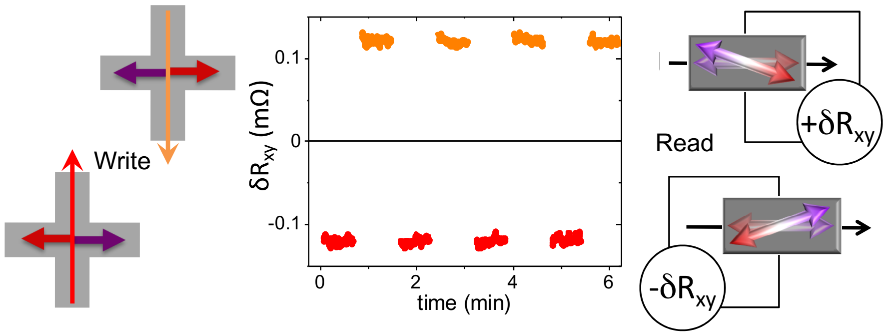

Figure 6: Writing current pulses along the $\pm y$-direction (red/yellow arrows) are applied to set the Néel vector along the $\pm x$-axis. 180° reversal of the Néel order is probed by the current-dependent resistance δR_{xy}, associated with the electrically induced deflection of antiferromagnetic moments (double-arrows) combined with AMR, for equilibrium antiferromagnetic moments (semi-transparent double-arrows) aligned with the x-axis of the probing current. From Ref. [5]

Objective O1.3: Non-volatile retention. The envisaged applications of the multilevel antiferromagnetic bit cells are not, at least in short-term, in the non-volatile high-density computer memories. Instead, the initial targeted area is in specialized embedded applications for, e.g., the IoT technologies. The perceived components comprise multi-level antiferromagnetic bit-cells where each integrates a memory-logic (e.g. counter) functionality or shows analogue (memristive, synaptic) characteristics. This concept does not impose the stringent requirements on retention and scalability of high-density computer memories. With this in mind, in most of our performed experiments the output signal is measured seconds after the pulse ($10^3 - 10^{10}$ larger times than the pulse length). This data retention time-scale is sufficient for a range of envisaged IoT applications utilizing the embedded antiferromagnetic components. Apart from this we have also initiated more systematic studies of the retention characteristics with the following key results:

- In CuMnAs devices, the 90° electrical switching signal often shows partial relaxation after turning the writing pulse off, as illustrated in Fig. 7. In the same microdevice that shows partial relaxation at room temperature, a non-relaxing retention is achieved by lowering the temperature by only ∼10deg (see Fig. 7 and more details in Ref. [4]). This clearly leaves space for materials and device optimization towards high retention in CuMnAs based devices at room-temperature.

- In Mn_2Au devices, we achieved a stable 90° switching signal at room-temperature without performing dedicated materials optimization (more details in Ref. [7]).
- In CuMnAs devices, the 180° electrical switching is stable at room-temperature, showing no sign of decay over the studied 25 hour probing time (see Fig. 8 and more details in Ref. [5]).

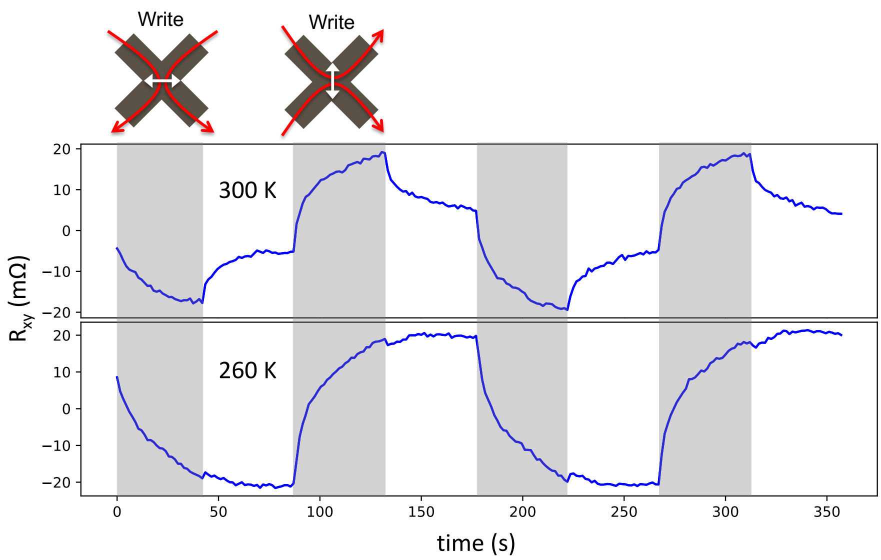

Figure 7: Examples of switching by trains of 30 pulses within 45 s with individual pulse-length of 100 μs and alternating orthogonal writing current directions (grey regions), and of signal relaxation within 45 s with the pulse-train turned off (light regions) at (A) base temperature 300 K and writing current density 1.6×10^7 Acm^{-2} and (B) base temperature 260 K and writing current density 2.2×10^7 Acm^{-2}. From Ref. [4]

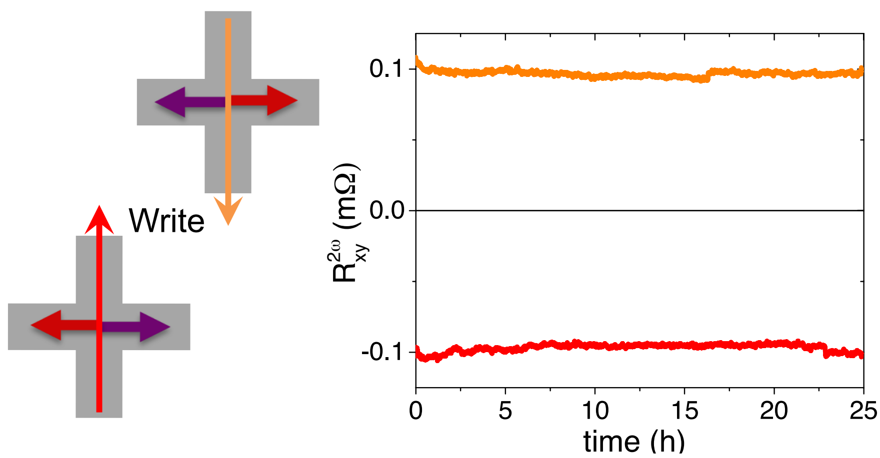

Figure 8: Same as Fig. 6 for one writing pulse along $+y$-axis and one subsequent pulse along $-y$-axis and 25 hour measurement of the stability of the corresponding probing signals. From Ref. [5]

Objective O1.4: Memory-logic multi-level bit cells. A highly reproducible multi-level characteristics of our antiferromagnetic memory-cells represents an attractive feature for envisaged memory-logic or neuromorphic applications. We have performed a systematic study of the current-controlled multi-level switching with the following key results:

- In CuMnAs devices, 90° multi-level switching can be realized both in a symmetric or asymmetric switching mode, as illustrated in Fig. 9 (for more details see Ref. [1]).
- The output signal can be controlled by the length of individual writing pulses (electrical pulsing tested in the range of 250 ps – 10 ms), amplitude of the writing current (tested in the range of $\sim 10^6 - 10^8$ Acm^{-2}), and number of pulses (tested up to ~ 1000 pulses applied in one direction). Typical data with the highlighted reproducibility are shown in Fig. 10 and for more details see Ref. [1].
- Analogous multi-level switching characteristics is observed in Mn_2Au devices (see Fig. 11 and Ref. [7]).
- The multi-level electrical switching characteristics is associated, based on XMLD-PEEM measurements, with antiferromagnetic multi-domain reconfigurations. Within the limited beam-time available till month-12, we where able to observe a range of domain structures in CuMnAs films, with individual domain sizes ranging from ~ 10 nm to ~ 10 μm, which are likely associated with different growth or post-growth treatments of the films or device structures. Illustrative XMLD-PEEM data are shown in Fig. 12, for more details see Ref. [8], and a more systematic study linking the material and device preparation protocols with the domain structure and electrical switching characteristics is underway.

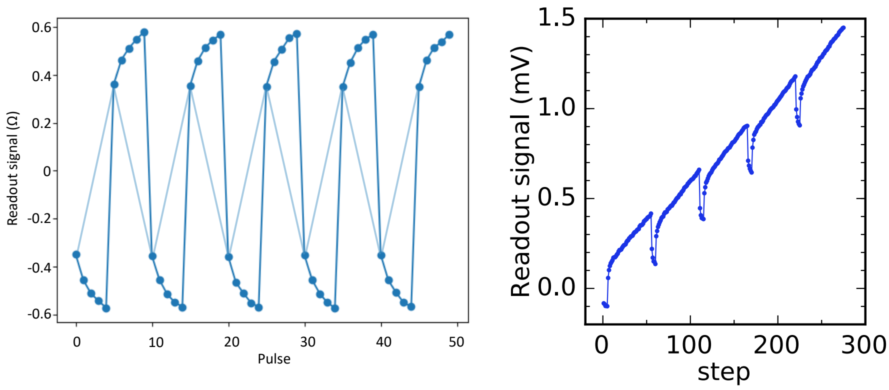

Figure 9: Left: Analogue (memristive, synaptic) mode of an antiferromagnetic memory cell with AMR readout. Five writing pulses in one direction are followed by five pulses in the orthogonal direction. Right: Analogous to the left panel with four pulses followed by fifty orthogonal pulses. From Refs. [6, 1]

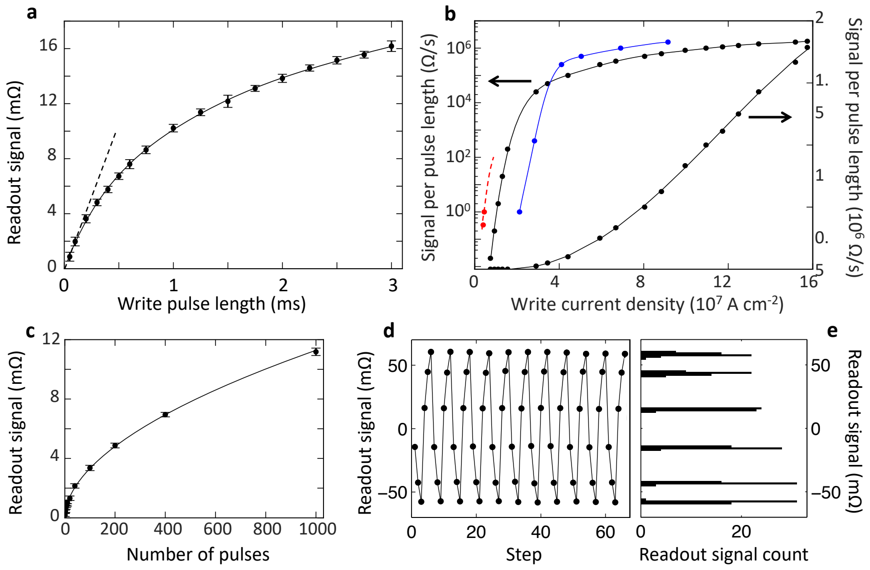

Figure 10: (**a**) Readout signal of a 4 µm CuMnAs/GaAs device as a function of the applied write-pulse length at a fixed current density of 1.2×10^7 Acm^{-2}. The initial linear slope of the dependence (signal per pulse length ratio) is highlighted by the dashed-line linear fit. (**b**) Readout signal per write-pulse length as a function of the write current density, for 30 µm CuMnAs/GaP (red), 4 µm CuMnAs/GaAs (black), and 2 µm CuMnAs/GaP (blue) devices. (**c**) Readout signal as a function of the number of pulses in the train of pulses for the individual pulse length of 250 ps and writing current density 16×10^7 Acm^{-2} in a 4 µm CuMnAs/GaAs devices. (**d**) Multi-level switching in the device fabricated from CuMnAs/Si. Three pulses are applied along the [100] direction followed by three pulses along the [010] direction with current density of 2×10^7 Acm^{-2} and pulse length 100 µs. Right: Histogram of the six different states, obtained from 50 repetitions of the 3+3 pulse sequence. From Ref. [1]

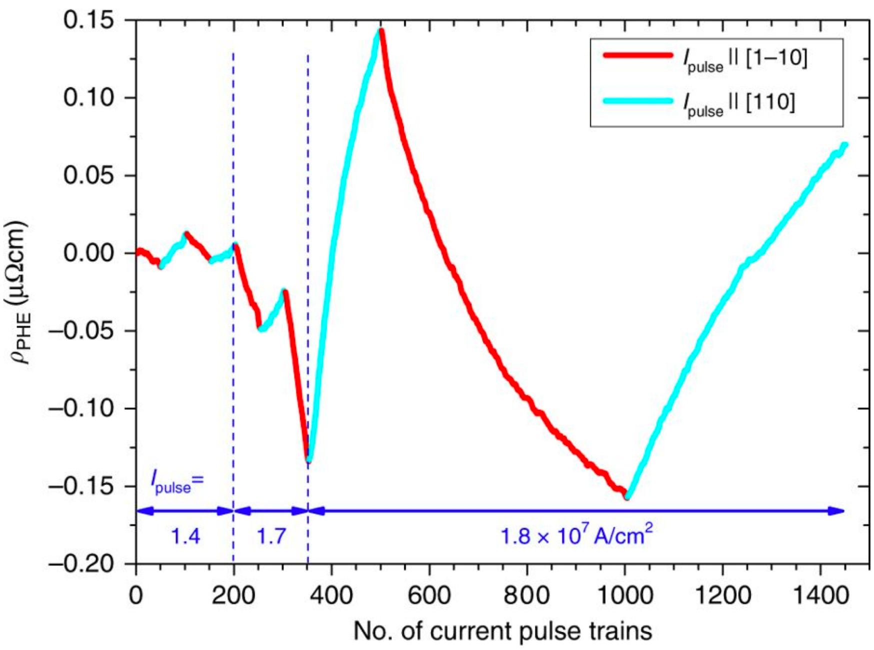

Figure 11: Multilevel orthogonal (red/cyan) switching in a Mn_2Au bit cell. From Ref. [7]

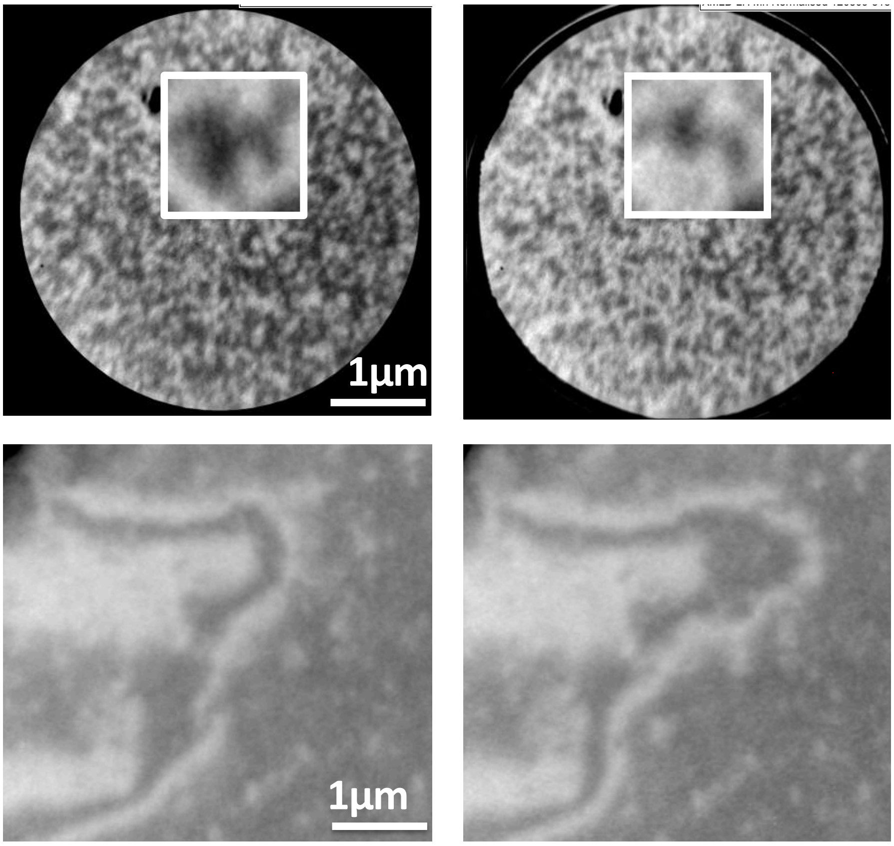

Figure 12: Light/dark contrast corresponding to domains in CuMnAs with orthogonal Néel vector directions imaged by XMLD-PEEM technique. Top panels: two states written by orthogonal current pulses in a material with small domains (insets: enlarged 10×). Bottom panels: 180° domain wall displacement in two states written by current pulses with opposite polarity in a material with larger domains. From Ref. [6, 8]

Objective O1.5: Insensitivity to magnetic fields and absence of stray fields. Prior to device fabrication, the antiferromagnetic films are tested by magnetization experiments to verify zero (negligible) net magnetic moment in the film. The electrical switching is also routinely tested to be insensitive to strong ($\sim$ 10 T) magnetic fields. The observed small field-dependent contributions to the switching signal are below 1% of the signal achieved by the current-induced spin-orbit torque. High magnetic field experiments in the tens of Tesla range are underway.

Objective O1.6: Compatibility with microelectronics. To demonstrate the realistic prospect of transferring the only very recent scientific discovery [3] from 2016 of the electrical control of antiferromagnets from laboratory experiments to future practical IoT applications, we have initiated the following steps:

- We have implemented the multi-level CuMnAs bit-cells in a standard printed circuit board (PCB). The simplicity of the circuitry sufficient to operate the antiferromagnetic bit-cell is highlighted in Fig. 13 (for more details see Ref. [1]). Apart from the CuMnAs memory chip, it contains only standard transistors and a microcontroller, powered by a 3 V USB 2.0 socket, for sending the write/read voltage signals. The device, which we call "AFMEM1.0", operates at ambient conditions and shows highly reproducible multi-level switching signals with a single readout step and no additional output data processing.
- At the premises of the Czech Academy of Sciences we have set up a development site of IoT ap-

plications, namely of a spintronic vehicle detection technology Spinwire® for smart cities (see Fig. 14 and http://147.231.58.18/mgaraze/). It is based on sensing changes of the geomagnetic field. The commercial version of our Spinwire® technology (https://www.spinpark.cz/) operates on the basis of a digital deterministic algorithm translating the vehicle-induced changes of the geomagnetic field into the traffic/parking data. On the Czech Academy of Sciences testing site, we have initiated the development of a software-emulated neuromorphic detection algorithm based on a conventional CMOS hardware.

- We have initiated the circuit designing of a proof-of-concept realization of an artificial neural network circuit with antiferromagnetic hardware synapses. A schematic diagram of this "AFMEM2.0" circuit, comprising a neuron equipped with analogue antiferromagnetic synapses ($R_{1,2,3,...}$) and threshold (R_{f}), is shown in Fig. 15, together with the weighted-input-sum and output firing functionality. For our specific IoT application, the input voltages represent signals from the geomagnetic field sensors. From our initial tests of the software-simulated neuromorphic algorithm based on back-propagation supervised training, the system is operational starting from four input signals and three layers of neurons. This allows us to construct the proof-of-concept AFMEM2.0 board with discrete antiferromagnetic synapses. All other parts will be standard circuit elements.

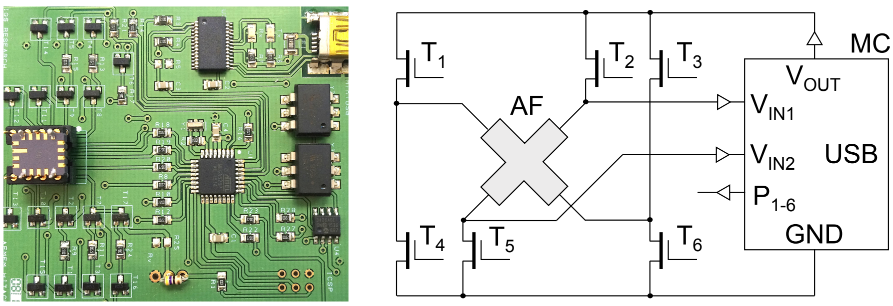

Figure 13: Left: Picture of the PCB with the chip containing the antiferromagnetic bit cell. Right: Schematics of the circuitry controlling the write/read functions. Microcontroller (MC) supplies the antiferromagnetic bit-cell circuit through its adjustable voltage output $\mathrm{V_{OUT}}$; different writing and reading configurations are realized by switching transistors $\mathrm{T_1}$ to $\mathrm{T_6}$ controlled by digital outputs $\mathrm{P_1}$ to $\mathrm{P_6}$ of the MC; transversal voltage is sensed differentially by analogue voltage inputs V_{IN1} and V_{IN2} of the MC. GND labels ground. From Ref. [1]

Figure 14: IGS development site for IoT applications (Spinwire® vehicle detection technology) at the Czech Academy of Sciences.

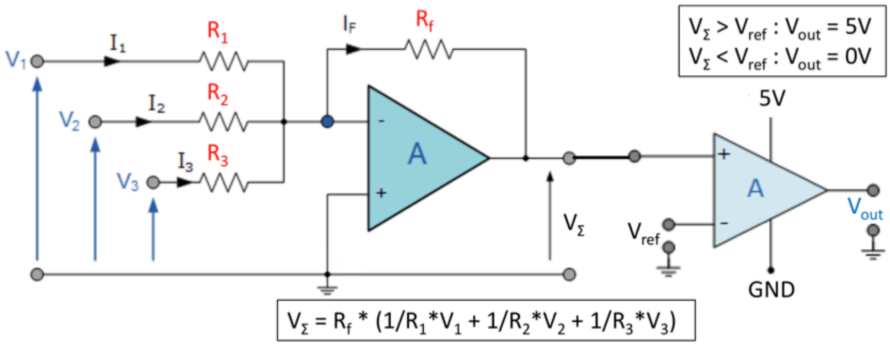

Figure 15: A simplified schematics of the circuit representation of a neuron with analogue synaptic weights ($R_{1,2,3,\ldots}$), analogue threshold (R_{f}), and input ($V_{1,2,3,\ldots}$) and output voltages (V_{out}).

Other antiferromagnetic materials CuMnAs films grown by molecular beam epitaxy and Mn_2Au films grown by sputtering are the key materials underpinning our most advanced research directions towards the multi-level antiferromagnetic bit cells. However, as planned in the ASPIN project, we have initiated investigation of possible alternative antiferromagnetic materials. In particular, we have focussed on non-collinear antiferromagnets of the Mn_3X family with the following initial results:

- We have shown that, apart from the anomalous Hall effect, non-collinear antiferromagnets such as Mn_3Sn and Mn_3Ir are analogous to ferromagnets in yet another aspect: the charge current in these materials is spin-polarized. We have illustrated the existence of the spin-polarized current by performing ab initio microscopic calculations and by analyzing the symmetry. Based on the spin-polarized current we have proposed an antiferromagnetic tunneling junction, analogous in functionality to the conventional ferromagnetic tunneling junction (see Fig. 16 and for more details Ref. [9]).
- We have performed initial sputtering growth and characterization of the structural and magnetic properties of noncollinear antiferromagnetic Mn_3Sn thin films heteroepitaxially grown on Y:ZrO2 (111) substrates with a Ru underlayer. The Mn_3Sn films were crystallized in

the hexagonal D019 structure with c-axis preferred (0001) crystal orientation. These initial Mn_3Sn films are discontinuous, forming large islands of approximately 400 nm in width. However, they are chemically homogeneous and characterized by a nearly perfect heteroepitaxy. These results show that Mn_3Sn films are potentially attractive materials for further exploration in antiferromagnetic spintronics (see Fig. 17 and for more details Ref. [10]).

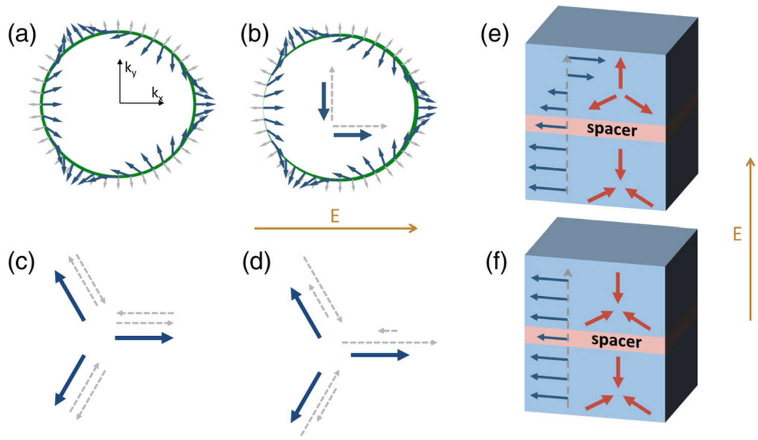

Figure 16: Models of Fermi level spin textures, spin-polarized current and tunnel junction in non-collinear antiferromagnets. From Ref. [9]

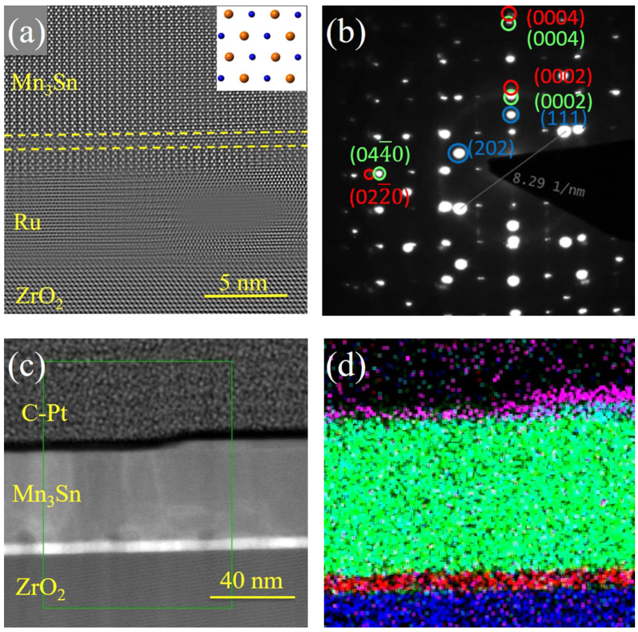

Figure 17: (a) Cross-section HRSTEM image of the 40 nm Mn3Sn film grown on Y:ZrO2 substrate with a 5 nm Ru underlayer. The inset illustrates the scheme of the Mn3Sn crystal lattice, where the large orange spheres and the small blue spheres correspond to the Sn and Mn atoms, respectively. (b) SAED pattern showing the diffraction spots from Mn3Sn (green open circles), Ru (red open circles), and Y:ZrO2 (blue open circles). (c) Cross-section HAADF-STEM image, where the green box denotes the area where chemical mapping was performed. (d) Elemental mapping of Zr (blue), Ru (red), Mn (green), Sn (light blue), and Al (purple). From Ref. [10]

1.2.2 Milestone M1 (month 12): Bit-cells for proof-of-concept device

From the above description of results achieved till month-12 of the ASPIN project we can conclude that we have reached the Milestone M1 as originally anticipated in the proposal: *"At milestone M1, specifications will be completed and validated for the multi-level AF bit cells with electrical writing/readout. At this point strategic plans will be refined and, if necessary, a correction feedback relayed to materials growth, device fabrication and modelling in order to choose the optimal path towards (i) the WP1 proof-of-concept AF memory-logic component for testing in IoT, and (ii) the WP2 opto-electrical AF devices for ultra-fast (ps) operation."*

1.2.3 Work Package WP2, Objective O2: Picosecond optics

Contributing teams:

- IOP: GaMnAs test materials growth, CuMnAs THz device fabrication, THz absorption measurements, theory
- NOT: CuMnAs materials growth and characterization
- MPG: THz switching experiments
- CHU: time and spatially resolved magneto-optical set-up and testing in GaMnAs
- JGU: theory

Objective O2.1: Built-in photoconductive switches. In our initial experiments, we have detected THz electric fields emitted from our device structures as depicted in Fig. 2 when directly illuminated by a focused laser beam at the semiconductor-substrate sub-gap wavelengths and simultaneously electrically biased. These results can be potentially utilized for in-situ THz excitation of the CuMnAs antiferromagnet. Moreover, a weaker THz emission from the non-centrosymmetric CuMnAs film itself when the writing electrical bias is switched off can be potentially used for time-resolved THz detection of the switching of the antiferromagnetic memory device. These preliminary results will be further tested and exploited.

Objective O2.2: Time-resolved optical readout. Following our earlier work on optical magnetic-linear-dichroism detection of the Néel vector in CuMnAs from before the ASPIN project submission (see Ref. [11]), we have designed and experimentally realized a pump-probe experimental setup with a high temporal and spatial resolution combined with a wide-field magneto-optical microscope (for details see Fig. 18 and Ref. [12]). We have already performed successful test experiments on time-resolved domain imaging in a related ferromagnet GaMnAs (see Ref. [12]) and initial experiments in CuMnAs are currently underway.

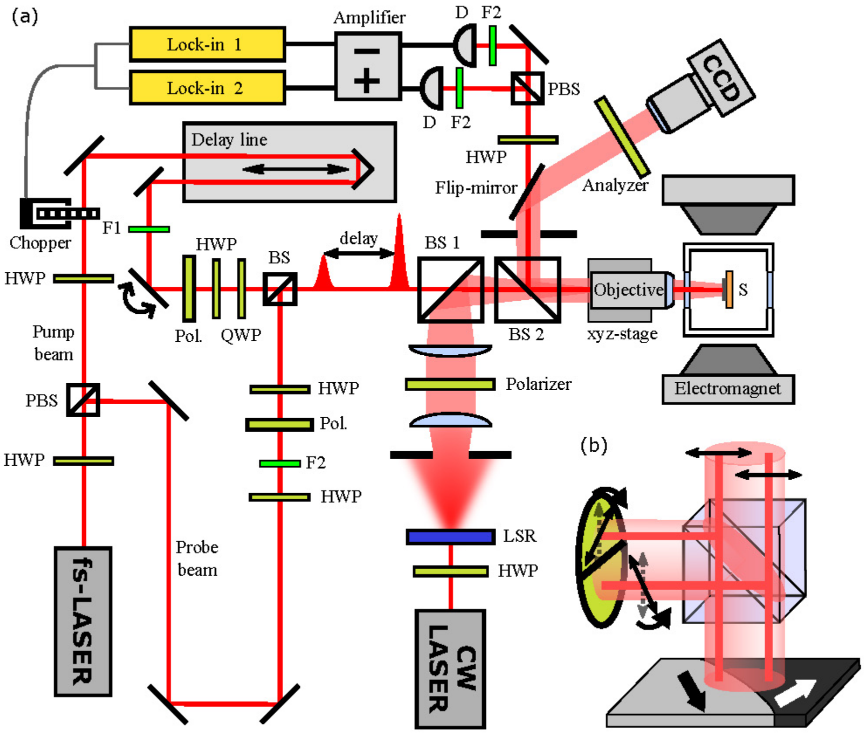

Figure 18: Pump-probe experimental setup with a high spatial resolution combined with a wide-field MO microscope. (a) A sketch of the experimental layout. Pump-probe experiment: Each pulse emitted by a femtosecond (fs) laser is divided into pump and probe pulses by a polarizing beam splitter (PBS) with an intensity ratio set by a half-wave plate (HWP). Another pair of HWP and polarizer is used to set the intensity in each beam. Filters F1 and F2 are used to spectrally separate the pump and probe beams. Sets of polarizer, half-, and quarter-wave plate (QWP) define the polarization of pump and probe pulses which are then merged by a beam splitter (BS), with a variable mutual time delay set by a delay line, and focused on the sample (S) by an objective lens. The sample is placed in an optical cryostat between the poles of an electromagnet. Beams reflected from the sample are directed by BS 2 toward an optical-bridge detection system where the pump pulses are suppressed by filters F2. MO microscope: HWP and polarizer are used to set intensity and vertical (s) polarization of light emitted by a continuous (cw) laser. A laser speckle reducer (LSR) suppresses interference effects due to the laser coherence. The optical system creates nearly parallel beam illuminating the sample, and the reflected light is guided by an optional flip-mirror through an analyzer to a CCD camera. (b) The working principle of a wide-field MO microscope. The polarization plane of the light reflected from places with different orientations of magnetization in the sample plane is rotated by a different angle resulting in a different intensity transmitted through the analyzer. From Ref. [12]

Objective O2.3: THz excitation/detection. The speed of writing of state-of-the-art ferromagnetic memories is physically limited by an intrinsic GHz ferromagnetic resonance threshold. We have experimentally demonstrated at room temperature that the speed of reversible electrical writing in a memory device as depicted in Fig. 2 can be scaled up to THz using the CuMnAs antiferromagnet. Since the antiferromagnetic resonance threshold is shifted to the THz scale, the same current-induced spin-torque mechanism can be responsible for the switching in our memory devices throughout the twelve orders of magnitude range of writing speeds from Hz to THz (writing pulse lengths from seconds down to picoseconds). The results summarized below and described in detail in Ref. [4] thus opens a path towards the development of memory technology, including the multi-level (memristive or synaptic) characteristics, reaching the elusive THz band:

- To establish the feasibility of extending the writing speed in antiferromagnets to the THz band, we have compared our ultra-short writing pulse experiments to the results obtained with longer writing pulses in the same device structure (see Fig. 19). For our experiments with ps pulses, we employed a non-contact technique for generating the ultra-short current pulses in the memory cell. We applied free-space THz electro-magnetic pulses whose linear polarization can be chosen along two orthogonal directions to generate the reversible 90° switching. The wave-form of the incident electric-field transient is shown in Fig. 19. We applied a bipolar wave-form of the writing pulses also in the contact set-up with longer (μs) pulses to explicitly highlight the correspondence to the non-contact, ps-pulse measurements.
- Fig. 20 presents typical measured data for μs writing pulses delivered by the contact method. The data were obtained for an applied writing current density $j = 3 \times 10^7$ Acm^{-2} and a writing pulse repetition rate of 1 Hz. Analogous reversible switching traces can be written in the same CuMnAs memory cell structure by ps-pulses, as also shown in Fig. 20. Here the current density generated by the THz pulse was increased to $j \approx 2.7 \times 10^9$ Acm^{-2}.
- Measured THz absorption spectrum together with Comsol device simulations were used to calibrate the relationship between the incident THz field and the generated electrical current density in the CuMnAs memory cell (see Fig. 21 and Ref. [4] for more details on these calibration experiments and simulations).
- The switching Joule energy for the ps-pulses remains the same as in the ns-range, i.e. $\sim$ kJcm^{-3} (see Fig. 3), making these ultra-fast switching experiments feasible.
- We have theoretically studied dynamics of antiferromagnets induced by simultaneous application of dc spin current and ac charge current, motivated by the requirement of all-electrically controlled devices in the terahertz (THz) gap (0.1-30 THz). We have shown that ac electric current, via antiferromagnetic spin-orbit torques, can lock the phase of a steady rotating Néel vector whose precession is controlled by the dc spin current. In the phase-locking regime the frequency of the incoming ac signal coincides with the frequency of auto-oscillations, which for typical antiferromagnets falls into the THz range. We show how the incoming ac signal can be detected and formulate the conditions of phase locking in the antiferromagnetic spintronic THz detector (for more details see Ref. [13]).

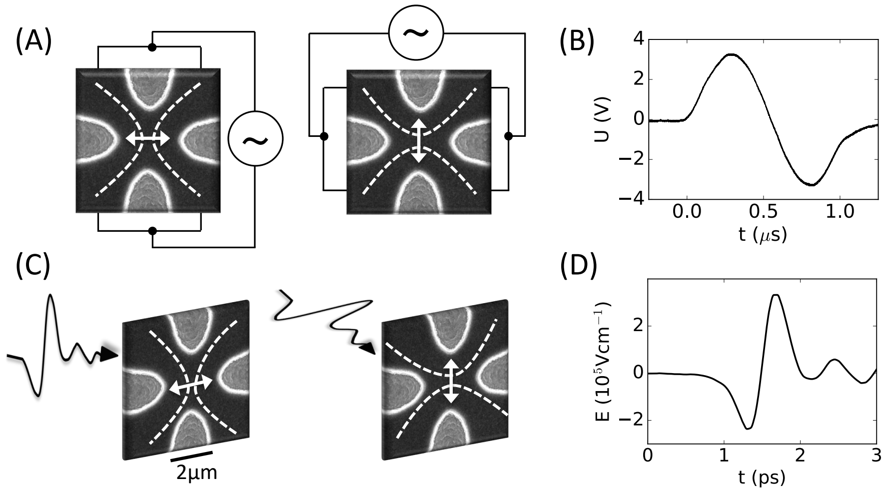

Figure 19: (A) Electron microscopy image of the cross-shape bit cell and schematics of the reversible writing by electrical pulses of two orthogonal current directions delivered via wire-bonded contacts. White dashed lines illustrate electrical current paths and white double-arrows the corresponding preferred Néel vector orientations. (B) Wave-form of the applied μs electrical pulses. (C) Schematics of the reversible writing by THz electric-field transients whose linear polarization can be chosen along two orthogonal directions. (D) Wave-form of the applied ps radiation pulses. From Ref. [4]

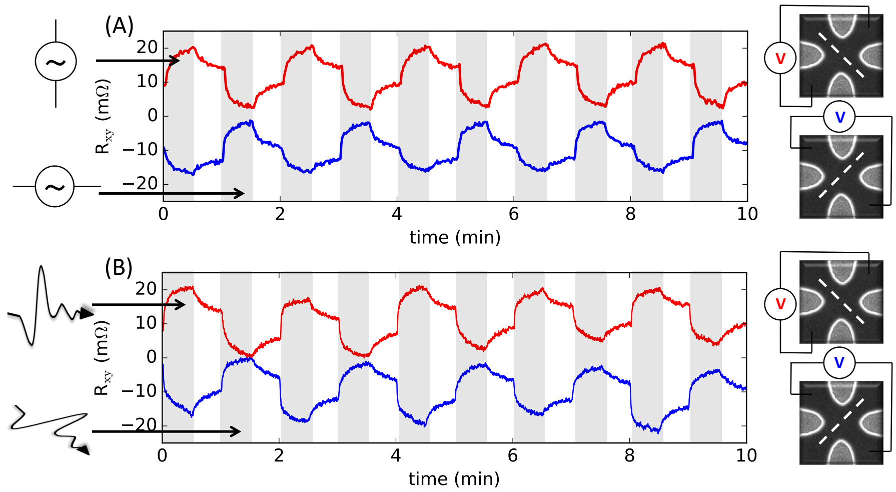

Figure 20: (A) Reversible multi-level switching by 30 s trains of μs electrical pulses with a Hz pulse-repetition rate, delivered via wire-bonded contacts along two orthogonal directions. The applied writing current density in the 3.5 μm-size CuMnAs/GaAs cell is 3×10^7 Acm^{-2}. Intervals with the pulse trains turned on are highlighted in grey and the two orthogonal current-directions of the trains are alternating from one interval to the next. Electrical readout is performed at a 1 Hz rate. Right insets show schematics of the transverse AMR readout. White dashed lines depict readout current paths. (B) Same as (A) for ps-pules with a kHz pulse-repetition rate. The writing current density in the 2 μm-size CuMnAs/GaAs bit cell recalculated from the amplitude of the applied THz electric-field transient is 2.7×10^9 Acm^{-2}. Electrical readout is performed at a 8 Hz rate. From Ref. [4]

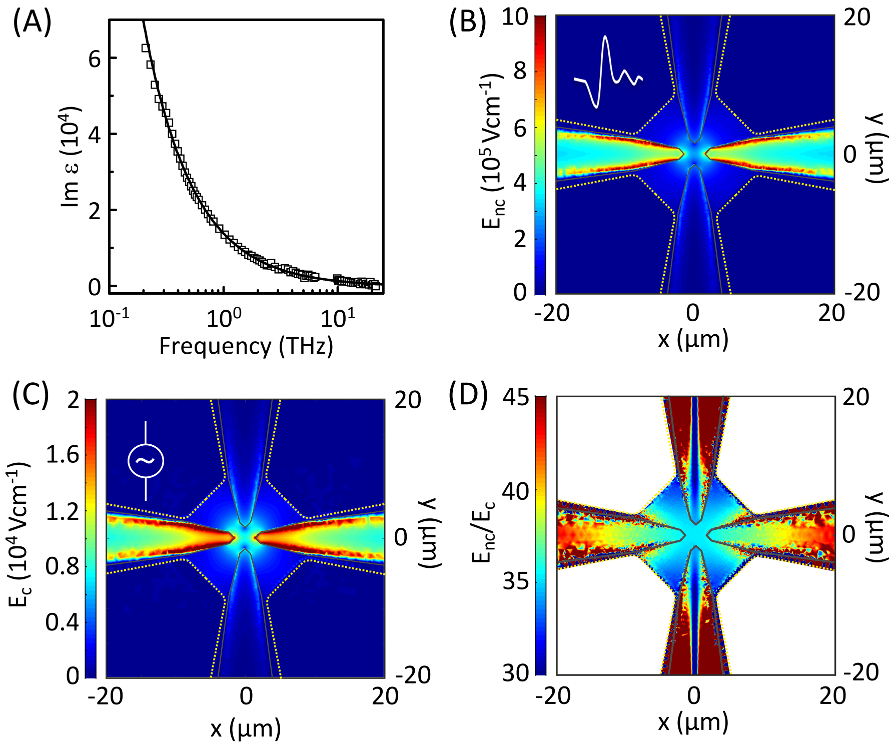

Figure 21: (A) Measured frequency-dependent imaginary part of the dielectric function (squares) and fitted expression $\mathrm{Im}\,\varepsilon = \sigma_0/\omega\varepsilon_0$ (line) with the dc conductivity $\sigma = 8 \times 10^3\ \Omega^{-1}\mathrm{cm}^{-1}$. (B) Numerical simulation of the electric field distribution in the device in the non-contact set-up for a peak incident THz field of 10^5 Vcm^{-1} polarized along the y-axis. (D) Same as (C) in the contact set-up for a voltage of 7 V applied between the top and bottom Au-contacts. (D) Ratio of the electric fields in panels (B) and (C). From Ref. [4]

1.2.4 Milestone M2 (month 30): Ultra-fast ps writing

From the above description of results achieved till month-12 of the ASPIN project we can conclude that we have reached the Milestone M2 which was originally anticipated to be reached at month-30: *"At milestone M2, the ultra-fast (ps) writing will be experimentally validated. At this point we will critically assess the efficiency of THz pulses for the ultrafast writing of antiferromagnets. If necessary, a correction feedback relayed to materials growth, device fabrication and modeling will take place in order to choose the optimal path towards implementing the ultra-fast switching in multi-level antiferromagnetic memory-logic bit cells."*

As to the follow-up research we point out that a THz-speed memory, whether realized in antiferromagnets or another alternative system that may be discovered in the future, is only one of the many components that need to be developed to make true THz electronics and information technologies a realistic prospect. In the meantime, however, the ultra-fast writing of antiferromagnetic bit cells can be potentially exploitable without separate THz-speed processors. The multi-level memristive-like characteristics allows for integrating memory and logic (neuromorphics) within the antiferromagnetic bit cell. Future low-noise experiments with THz writing pulses and repetition rates spanning a broad range up to THz will establish the feasibility and versatility of this autonomous THz memory-logic concept built within the antiferromagnetic bit-cells, that requires no separate processor to perform the THz-speed logic operation.

1.2.5 Work Package WP3, Objective O3: Topological Dirac phases

Contributing teams:
- IOP: theory in CuMnAs
- MPG: theory in Ti_2MnAl
- JGU: magnetoresistance measurement and theory in Mn_2Au

Objective O3.1: Topological magneto-transport phenomena. Since traditionally antiferromagnets have been regarded as materials of little utility, their dedicated extensive materials research is yet to be performed. This applies in general to the broad family of 122 magnetic point groups allowing for the antiferromagnetic order, which contrasts with the much narrower family of 31 magnetic point groups of the heavily explored ferromagnets (see e.g. our recent review [14]. The rich symmetry landscape of antiferromagnets is accompanied by topology properties that are unparalleled in ferromagnets. In this context we have obtained the following results:
- Based on symmetry analysis and first-principles calculations we have shown that CuMnAs and Mn_2Au are an illustration in which the combined PT-symmetry (space and time inversion) in the magnetic lattice allows for the formation of topologically protected, four-fold degenerate Dirac points, which are prohibited by symmetry in all ferromagnetic point groups. (See Fig. 22 and Refs. [15, 7] for more details.)
- The same PT-symmetry allowing for the Dirac points is also behind the presence of the efficient current-induced spin-orbit torque in CuMnAs or Mn_2Au [15]. Since the topological protection of the Dirac points depends on the orientation of the Néel vector, the spin-orbit torque switching can result in opening and closing of the gap at the Dirac point and in the corresponding topological AMR [**15**].
- In our experimental and theoretical study we have already associated the observed large crystalline components of the AMR in Mn_2Au with the opening and closing of the gap at the Dirac point near the Fermi level (see Fig. 23 and for more details Ref. [7]).
- We have predicted huge topological AMRs due to metal-insulator transition in antiferromagnetic semimetals whose Dirac points with the tuneable gap are at the Fermi level. An example here is the orthorhombic CuMnAs (for more datails see Ref. [15]).
- We have predicted a magnetic Weyl semimetal in the inverse Heusler Ti_2MnAl which is a compensated ferrimagnet with a vanishing net magnetic moment and a Curie temperature of over 650 K. Despite the vanishing net magnetic moment, we obtained a large intrinsic anomalous Hall effect of about 300 S/cm. It derives from the Berry curvature distribution of the Weyl points, which are close to the Fermi level and isolated from trivial bands (for more details see Ref. [16]).

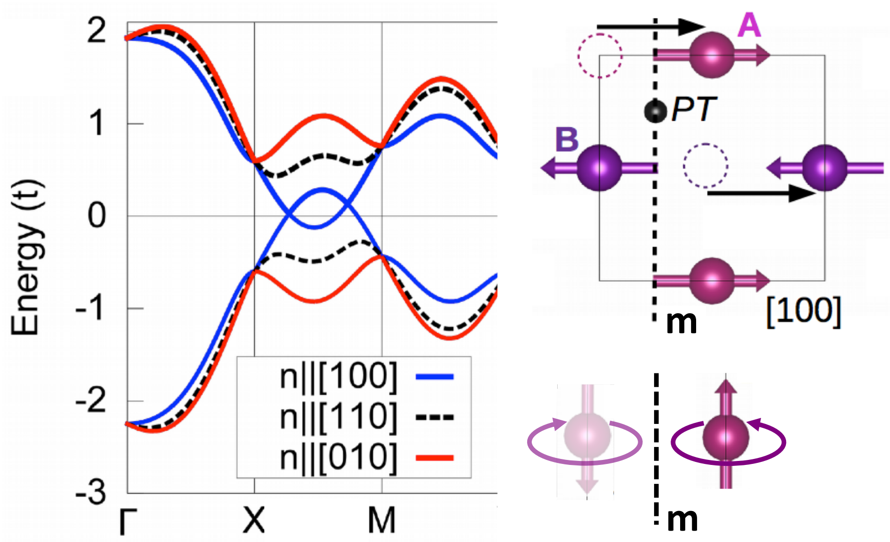

Figure 22: Left: Band dispersion of a minimal antiferromagnetic model illustrating the control of the protection of the Dirac point by Néel vector direction. Right: Top view of our quasi-2D antiferromagnetic model highlighting the non-symmorphic glide mirror plane symmetry that protects the Dirac point when the magnetic moments are orthogonal to the mirror plane. The protection is lifted when the moments point parallel to the mirror plane. From Ref. [15]

Objective O3.2: Band-structure spectroscopy of spin control of Dirac/Weyl fermions. We have prepared suitable CuMnAs and Mn_2Au films for ARPES band-structure spectroscopy measurements and the experiments are currently underway.

1.2.6 Milestone M3 (month 30): Topological transport effects

From the above description of results in Mn_2Au, where we identified the topological contribution to the measured AMR, we can conclude that we have, at least partially, reached the Milestone M3 which was originally anticipated to be reached at month-30: *"At milestone M3, topological magneto-transport phenomena will be experimentally validated. At this milestone a strategic decision will be made in choosing the most promising topological Dirac/Weyl AF for implementing the topological effects in writing and/or readout of AF bit cells. If necessary, a correction feedback will be relayed to materials growth, spectroscopy and transport measurements, and modeling to search for the most efficient topological effects for writing/readout."*

In the follow-up research we will focus on demonstrating the topological magneto-transport effects in a pristine form, instead of just a contribution to a non-topological magnetoresistance. In case of the topological AMR, e.g., this will require to realize systems with Dirac points at the Fermi level.

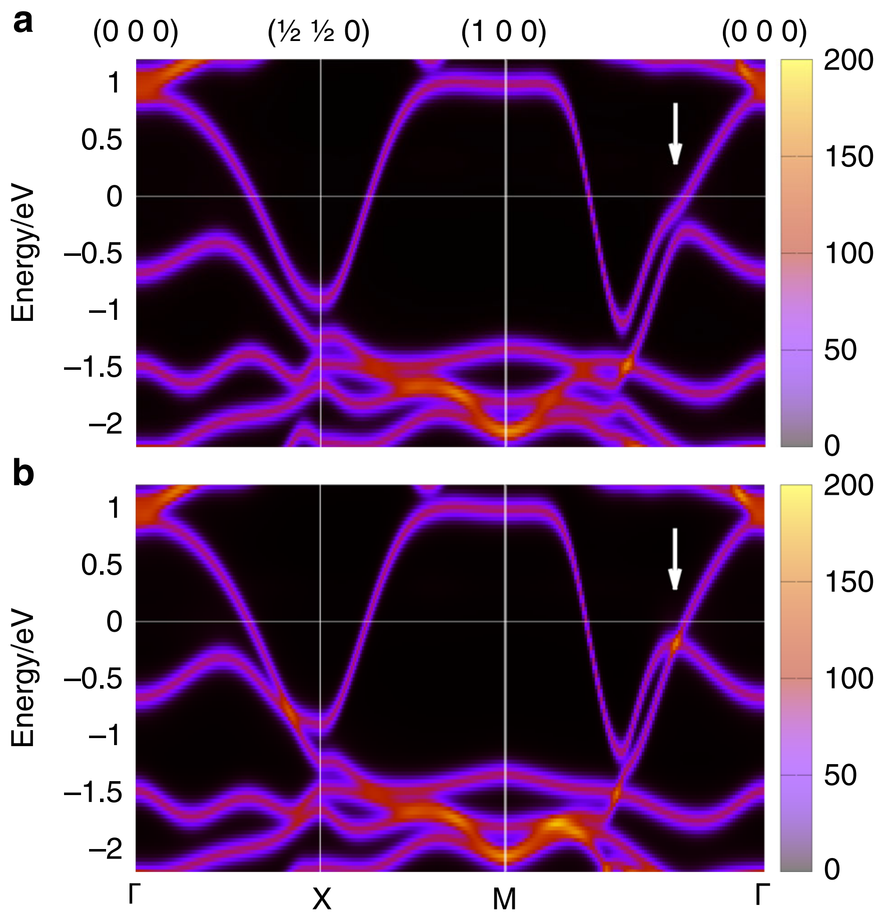

Figure 23: Bloch spectral function calculated in Mn_2Au for two orthogonal orientations of the Néel vector; changes near the Dirac crossing are highlighted by arrows. From Ref. [7]

1.3 Impact

The information on section 2.1 of the DoA (how the project will contribute to the expected impacts) is still relevant.

2 Update of the plan for exploitation and dissemination of result (if applicable)

N/A

3 Update of the data management plan (if applicable)

N/A

4 Follow-up of recommendations and comments from previous review(s) (if applicable)

N/A

5 Deviations from Annex 1 and Annex 2 (if applicable)

N/A

5.1 Tasks

The tasks for achieving critical objectives are implemented as planned and the available resources are adequate.

5.2 Use of resources

N/A

5.2.1 Unforeseen subcontracting (if applicable)

N/A

5.2.2 Unforeseen use of in kind contribution from third party against payment or free of charges (if applicable)

N/A

References

[1] Olejník, K. *et al.* Antiferromagnetic CuMnAs multi-level memory cell with microelectronic compatibility. *Nature Communications* **8**, 15434 (2017).

[2] Železný, J. *et al.* Relativistic néel-order fields induced by electrical current in antiferromagnets. *Physical Review Letters* **113**, 157201 (2014). `1410.8296`.

[3] Wadley, P. *et al.* Spintronics: Electrical switching of an antiferromagnet. *Science* **351**, 587–590 (2016). `1503.03765`.

[4] Olejník, K. *et al.* Terahertz electrical writing speed in an antiferromagnetic memory. *Science Advances* **4**, eaar3566 (2018). URL `http://advances.sciencemag.org/lookup/doi/10.1126/sciadv.aar3566`. `1711.08444`.

[5] Godinho, J. *et al.* Electrically induced and detected N\'eel vector reversal in a collinear antiferromagnet. *Nature Communications* **9**, 4686 (2018). URL `http://arxiv.org/abs/1806.02795`. `1806.02795`.

[6] T. Jungwirth, Antiferromagnetic spintronics, Plenary talk at ICM 2018, San Francisco.

[7] Bodnar, S. Y. *et al.* Writing and reading antiferromagnetic Mn2Au by Néel spin-orbit torques and large anisotropic magnetoresistance. *Nature Communications* **9**, 348 (2018). URL `http://www.nature.com/articles/s41467-017-02780-x`. `arXiv:1706.02482`.

[8] Wadley, P. *et al.* Current polarity-dependent manipulation of antiferromagnetic domains. *Nature Nanotechnology* **13**, 362–365 (2018). URL `http://www.nature.com/articles/s41565-018-0079-1`. `arXiv:1711.05146`.

[9] Železný, J., Zhang, Y., Felser, C. & Yan, B. Spin-Polarized Current in Noncollinear Antiferromagnets. *Physical Review Letters* **119**, 187204 (2017). URL `https://link.aps.org/doi/10.1103/PhysRevLett.119.187204`. `1702.00295`.

[10] Markou, A. *et al.* Noncollinear antiferromagnetic Mn3Sn films. *Physical Review Materials* **2**, 051001 (2018). URL `https://link.aps.org/doi/10.1103/PhysRevMaterials.2.051001`.

[11] Saidl, V. *et al.* Optical determination of the Néel vector in a CuMnAs thin-film antiferromagnet. *Nature Photonics* **11**, 91–96 (2017). `1608.01941`.

[12] Janda, T. *et al.* Voigt effect-based wide-field magneto-optical microscope integrated in a pump-probe experimental setup. *Review of Scientific Instruments* **89**, 073703 (2018). URL `http://aip.scitation.org/doi/10.1063/1.5023183`.

[13] Gomonay, O., Jungwirth, T. & Sinova, J. Narrow-band tunable terahertz detector in antiferromagnets via staggered-field and antidamping torques. *Phys. Rev. B* **98**, 104430 (2018). URL `http://arxiv.org/abs/1712.02686https://link.aps.org/doi/10.1103/PhysRevB.98.104430`. `1712.02686`.

[14] Šmejkal, L. & Jungwirth, T. Symmetry and topology in antiferromagnetic spintronics. In Zang, J., Cros, V. & Hoffmann, A. (eds.) *Topology in magnetism*, 267–298 (Springer International Publishing, 2018). URL `http://arxiv.org/abs/1804.05628`.

[15] Šmejkal, L., Železný, J., Sinova, J. & Jungwirth, T. Electric Control of Dirac Quasiparticles by Spin-Orbit Torque in an Antiferromagnet. *Physical Review Letters* **118**, 106402 (2017). `1610.08107`.

[16] Shi, W. *et al.* Prediction of a magnetic Weyl semimetal without spin-orbit coupling and strong anomalous Hall effect in the Heusler compensated ferrimagnet Ti2MnAl. *Physical Review B* **97**, 060406(R) (2018). `1801.03273`.